

# Machine learning for predicting the $B_z$ magnetic field component from upstream in situ observations of solar coronal mass ejections

M. A. Reiss<sup>1</sup>, C. Möstl<sup>1</sup>, R. L. Bailey<sup>2</sup>, H. T. Rüdisser<sup>3,4</sup>, U. V. Amerstorfer<sup>1</sup>,  
T. Amerstorfer<sup>1</sup>, A. J. Weiss<sup>1,4</sup>, J. Hinterreiter<sup>1,4</sup>, and A. Windisch<sup>3,5,6</sup>

<sup>1</sup>Space Research Institute, Austrian Academy of Sciences, Schmiedlstraße 6, 8042 Graz, Austria

<sup>2</sup>Zentralanstalt für Meteorologie und Geodynamik, Hohe Warte 38, 1190 Vienna, Austria

<sup>3</sup>Know-Center GmbH, Inffeldgasse 13, 8010 Graz, Austria

<sup>4</sup>Institute of Physics, University of Graz, Universitätsplatz 5, 8010 Graz, Austria

<sup>5</sup>Department of Physics, Washington University in St. Louis, MO 63130, USA

<sup>6</sup>RL Community, AI AUSTRIA, Wollzeile 24/12, 1010 Vienna, Austria

## Key Points:

- We hypothesize that upstream in situ measurements are sufficient to predict  $B_z$  in solar coronal mass ejections.
- We present a predictive tool that forecasts the minimum of  $B_z$  in an ICME with a MAE of 3.12 nT and a PCC of 0.71.

## Abstract

Predicting the  $B_z$  magnetic field embedded within ICMEs, also known as the  $B_z$  problem, is a key challenge in space weather forecasting. We study the hypothesis that upstream in situ measurements of the sheath region and the first few hours of the magnetic obstacle provide sufficient information for predicting the downstream  $B_z$  component.

To do so, we develop a predictive tool based on machine learning that is trained and tested on 348 ICMEs from Wind, STEREO-A, and STEREO-B measurements. We train the machine learning models to predict the minimum value of the  $B_z$  component and the maximum value of the total magnetic field  $B_t$  in the magnetic obstacle. To validate the tool, we let the ICMEs sweep over the spacecraft and assess how continually feeding in situ measurements into the tool improves the  $B_z$  prediction. Because the application of the tool in operations needs an automated detection of ICMEs, we implement an existing automated ICME detection algorithm and test its robustness for the time intervals under scrutiny.

We find that the predictive tool can predict the minimum value of the  $B_z$  component in the magnetic obstacle with a mean absolute error of 3.12 nT and a Pearson correlation coefficient of 0.71 when the sheath region and the first 4 hours of the magnetic obstacle are observed. While the underlying hypothesis is unlikely to solve the  $B_z$  problem, the tool shows promise for ICMEs that have a recognizable magnetic flux rope signature. Transitioning the tool to operations could lead to improved space weather forecasting.

## Plain Language Summary

At any time, our solar system is populated with interplanetary coronal mass ejections (ICMEs). Solar scientists and space weather forecasters track ICMEs when they are ejected from the Sun and follow their path into the vast reaches of interplanetary space. They do so because if an ICME hits Earth, it could damage our infrastructure such as power-grids and GPS satellites, which are a mainstay of our modern civilization. The possible damage is primarily determined by the magnetic field embedded within the ICME. The North-South magnetic field component,  $B_z$ , plays a decisive role, especially if it is pointing opposite to Earth's magnetic field. Currently we cannot predict  $B_z$  with sufficient accuracy. Scientists often refer to our limited predictive abilities as the  $B_z$  problem. Here we shine a new light on the  $B_z$  problem by developing a predictive tool based on machine learning that is trained and tested on 348 ICMEs. By feeding measurements of the ICME into machine learning algorithms, we find that our predictive tool can forecast the  $B_z$  component reasonably well. While our tool does not solve the  $B_z$  problem, it shows promise in forecasting and potentially mitigating the effects of ICMEs on our planet Earth and its inhabitants.

## 1 Introduction

The  $B_z$  component of the interplanetary magnetic field (IMF) largely determines the amount of energy and momentum transferred from the solar wind into the Earth's magnetosphere via magnetic reconnection at the dayside magnetopause (Dungey, 1961). Future knowledge of the  $B_z$  magnitude is integral for monitoring and predicting the energy input into the magnetosphere, ionosphere, and thermosphere. There is a current lack of forecasting capabilities, which is often referred to as the  $B_z$  problem. In essence, the field of space weather forecasting needs innovation to predict the north-south component ( $B_z$ ) of the IMF in near-Earth space during intense geoeffective events.

Key criteria for intense geoeffective events are extended periods of large southward  $B_z$ , which points opposite to the Earth's magnetic field (Gonzalez & Tsurutani, 1987).

The largest southward  $B_z$  disturbances in the IMF are found in coronal mass ejections (CMEs), plasma clouds with embedded magnetic fields that are expelled from the Sun into our solar system (see Webb & Howard, 2012, for a review). At any time, the heliosphere is filled with interplanetary coronal mass ejections (ICMEs) that interact with the prevailing ambient solar wind flows and fields. Most of the structure in the ambient solar wind comes from interacting fast and slow solar wind flows (Owens & Forsyth, 2013). Fluctuating magnetic fields in so-called stream interaction regions can also cause weak to moderate geomagnetic activity (Zhang et al., 2007; Kilpua et al., 2017). Although stream interaction regions are a driver of recurrent geomagnetic activity (Tsurutani et al., 2006), the most extreme geomagnetic disturbances are caused by large-scale  $B_z$  perturbations embedded within ICMEs (Echer et al., 2008). It is primarily during ICME events, when accurate  $B_z$  estimates are needed most, that the prediction thereof is most difficult and the  $B_z$  problem is most relevant.

Breakthroughs in the  $B_z$  problem are challenging for many reasons, including observational limitations (see Vourlidas et al., 2019). First, we can not accurately deduce the magnetic properties of CMEs such as magnetic field magnitude, topology, and helicity at the time of formation from observations alone. Radio and EUV off-limb imaging and spectroscopy can inform models, but we cannot measure these magnetic properties directly. Second, the coronal conditions within the Alfvén surface below approximately 20 solar radii, through which the CME evolves, are unknown. Due to the unknown condition in the corona, we do not understand the origin and early evolution of CMEs well enough to predict their magnetic structure (Vourlidas et al., 2013). Third, we cannot monitor the rotation, compression, deflection, and reconnection in interplanetary space with ambient solar wind fields, which influence the ICME magnetic field structure before they arrive at Earth.

When observations are limited, numerical models can provide insights into the physical conditions. One promising research avenue to tackle the  $B_z$  problem focuses on solving the three-dimensional equation of magnetohydrodynamics (MHD). Examples for MHD codes that incorporate the CME magnetic field structure are SUSANOO-CME (Shiota & Kataoka, 2016), AWSOM-SWMF (Jin et al., 2017), MAS (Török et al., 2018) and EU-HFORIA (Poedts et al., 2020). Although a full physical description is desirable, solving the  $B_z$  problem with MHD codes is challenging, as will be discussed later.

Without a definitive physical solution, we need to study new predictive tools that can enhance our predictive capabilities, and ideally, inform the boundary conditions of full physics-based models. Today's predictions of the  $B_z$  component at Earth rely on empirical relationships, statistical extrapolation, pattern recognition, machine learning algorithms, and more. Chen (1996) and Chen et al. (1997) first introduced the idea to use the coherence of magnetic flux ropes in ICMEs to predict their magnetic structure. They found that the  $B_z$  component at Earth can be predicted with lead times of up to 10 hours for well-defined magnetic clouds with a smooth field rotation. Kim et al. (2014) focused on early CME properties and updated their prediction by monitoring the solar wind conditions in space. In contrast, Savani et al. (2015) used remote sensing for predicting the magnetic field components in magnetic clouds at Earth. Here, their prediction relies on the categories introduced in Bothmer and Schwenn (1998) and Mulligan et al. (1998), among other things. More recently, Riley et al. (2017) developed a pattern recognition technique for predicting  $B_z$ , and Owens et al. (2017) used a past analogs method to predict the conditions in the ambient solar wind flow and geomagnetic indices at Earth. Salman et al. (2018) studied historic events to predict the southward interplanetary  $B_z$  periods after interplanetary shocks. Möstl et al. (2018) used solar observations to determine the initial state of the CME and assumes a self-similar expansion. In contrast, dos Santos et al. (2020) developed a deep neural network and an analytical flux rope model to identify the internal structure of ICMEs.

To date, however, scant attention has been paid to using upstream in situ measurements for predicting the  $B_z$  of the magnetic obstacle embedded within ICMEs at the Sun-Earth L1 point. In this study, we present a predictive tool based on machine learning and reduce the complexity of the  $B_z$  problem by predicting estimates of the  $B_z$  component for the whole magnetic flux rope, particularly  $\min(B_z)$  and  $\max(B_z)$ . We train, test, and validate the predictive tool on bulk plasma and in situ measurements from 348 ICMEs observed close to a heliocentric distance of 1 AU (Möstl et al., 2017; Möstl et al., 2020).

To simulate an operational space weather forecast, we feed in situ data into the predictive tool as if the ICMEs sweep over the spacecraft in an experimental real-time mode. We then assess how progressively adding data from the ICME sheath and parts of the magnetic obstacle improves the predictive skill. Since operational usage of our predictive tool needs a reliable real-time detection of ICMEs, we furthermore implement an existing automated ICME detection algorithm as introduced in Nguyen et al. (2019) and test its robustness and accuracy for the time interval under scrutiny. While the predictive tool combined with an automated ICME detection algorithm is far from solving the  $B_z$  problem, the framework shows reasonable first results in predicting estimates for the lower limit of the  $B_z$  component in ICMEs.

For the sake of consistency and clarity, we follow the definition in Nieves-Chinchilla et al. (2018) and use the term 'magnetic obstacle' to refer to the magnetic structure embedded in an ICME, which can deviate from in situ signatures of an idealized magnetic flux rope in L. Burlaga et al. (1981). We furthermore refer to the sheath as the region of compressed solar wind between the ICME shock front and the leading edge of the magnetic obstacle (Owens et al., 2005) and use the term ICME for the interval of disturbed solar wind conditions including the sheath region and the magnetic obstacle (Rouillard, 2011).

The paper consists of the following parts. After discussion of the data sources in Section 2, Section 3 outlines the machine learning approach, and Section 4 outlines the validation analysis. Section 5 presents the skill of the predictive tool, and Section 6 discusses the coupling of our tool with an existing ICME detection algorithm. Section 7 discusses our findings and outlines future perspectives, and Section 8 summarizes the study. Section 9 links to our publicly available online resources and the ICME catalog, in situ solar wind data, and the source code. All the machine learning algorithms are taken from the Python packages Scikit-learn and Keras, which are open-source, straightforward to use, and thoroughly tested.

## 2 Data

At any point in time, the heliosphere is populated by ICMEs, and their physical properties are continually recorded in ICME catalogs. In this study, we use an ICME catalog that was created during the HELCATS project (Möstl et al., 2017) and updated in Möstl et al. (2020). In particular, we use an ICME catalog called ICMECATv2.0, last updated on 2021 April 29. This version includes 558 ICMEs observed during the time interval 2007 January 1 to 2021 April 1. A large number of events, frequent updates, and open access (see Section 9) are the main advantages and the reasons for this choice.

**Figure 1** shows the probability distribution functions of physical properties of all the ICMEs in ICMECATv2.0. These properties include the mean and maximum of  $B_t$  in the magnetic obstacle, mean and minimum of  $B_z$  in the magnetic obstacle, mean of  $v_t$  in the ICME, and the duration of the sheath and magnetic obstacle. The value range of ICME and magnetic obstacle properties that we use for machine learning is as follows. The average duration of the sheath region is  $9.0 \pm 6.0$  h, and that of the magnetic obstacle is  $25.2 \pm 14.6$  h. The mean maximum value of  $B_t$  in the magnetic obstacle is  $14.3 \pm 7.6$  nT, and the mean minimum value of  $B_z$  in the magnetic obstacle is  $-9.4 \pm 6.8$  nT.

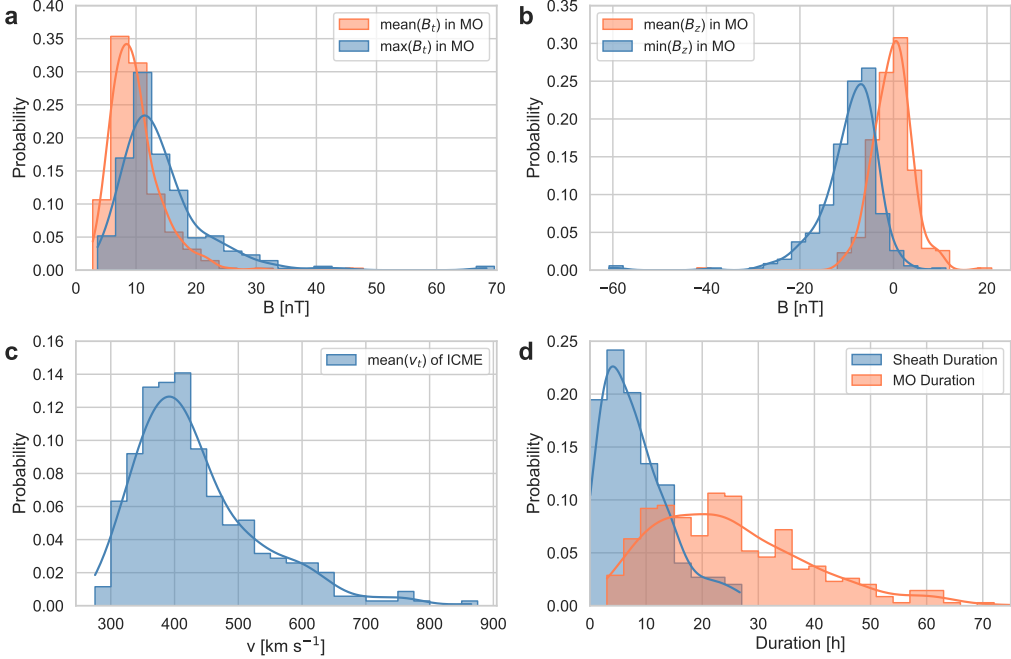


**Figure 1.** The probability distribution functions of the physical properties of 348 ICMEs under scrutiny. (a) The mean and maximum total magnetic field in the magnetic obstacle; (b) the minimum and mean  $B_z$  in the magnetic obstacle; (c) the mean bulk plasma speed in the ICME including the sheath and magnetic obstacle; and (d) the sheath and magnetic obstacle durations.

To train, validate, and test machine learning algorithms for predicting  $B_z$ , we use bulk plasma and in situ measurements close to a heliocentric distance of 1 AU. In particular, we study in situ measurements from the MFI and SWE instruments on the Wind spacecraft (Ogilvie et al., 1995; Lepping et al., 1995) and the IMPACT and PLASTIC instruments on the STEREO-A and STEREO-B spacecraft (Luhmann et al., 2008; Galvin et al., 2008). From the 558 ICMEs in ICMECATv2.0 observed by WIND, STEREO-A, and STEREO-B, we focus on 362 ICMEs (or 65%) that show either sheath region signatures or a density pileup in front of a magnetic obstacle. This selection results in 149 ICMEs in Wind, 135 ICMEs in STEREO-A, and 78 ICMEs in STEREO-B. After cleaning the data and removing events with too many missing data points in the measurements, we end up with 348 ICMEs, with 149 ICMEs in Wind, 123 ICMEs in STEREO-A, and 76 ICMEs in STEREO-B.

**Figure 2a** shows the heliocentric distance as a function of time for all the 348 selected ICMEs, with the color indicating the observing spacecraft. **Figure 2b** illustrates the maximum values of the total magnetic field  $B_t$  and the minimum of the  $B_z$  component in the magnetic obstacles. These two properties are the targets we want to predict. To do so, we train machine learning algorithms with ICME properties including the total magnetic field ( $B_t$ ), field components ( $B_x$ ,  $B_y$ ,  $B_z$ ), and the bulk plasma speed ( $v_t$ ), proton temperature ( $T_p$ ) and density ( $N_p$ ).

### 3 Machine Learning

To predict the  $B_z$  component in the magnetic obstacle embedded within an ICME, we train machine learning algorithms on the properties of 348 ICMEs. **Figure 3** illus-

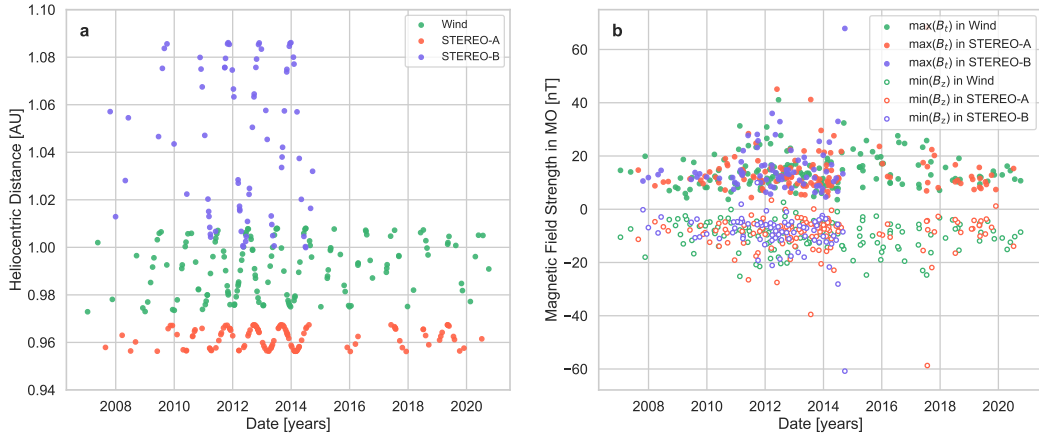


**Figure 2.** Properties of the 348 ICMEs in the catalog. (a) Heliocentric distance for each ICME event as a function of time, observed with Wind (green), STEREO-A (red), and STEREO-B (blue); (b) Maximum total magnetic field (filled circles)  $B_t$  and minimum value of the  $B_z$  component (open circles) in the magnetic obstacle (MO) of the ICME for each event as a function of time.

trates the main idea. Feature values computed in the ICME sheath region and parts of the magnetic flux rope (window delineated by green vertical lines) are used as input to machine learning to predict the minimum of the  $B_z$  component in the magnetic obstacle (red horizontal line). The three events in **Figure 3(a–c)** represent ideal, average, and poor  $B_z$  predictions of the tool, where the red horizontal lines show the prediction and the blue horizontal lines show the observation. The ideal, poor, and average examples correspond to an absolute error close to zero, the median absolute error, and the 75% percentile in the validation.

In the following, we introduce the predictive tool. To do so, we specify the features and targets, study different machine learning algorithms, split the ICME catalog into training and testing sets, perform hyperparameter tuning, and test the  $B_z$  prediction in an experimental real-time mode.

### 3.1 Features and Targets

We compute the features for machine learning from in situ plasma and magnetic field measurements of 348 ICMEs. In particular, we examine the timelines of 7 different physical properties ( $B_t$ ,  $B_x$ ,  $B_y$ ,  $B_z$ ,  $v_t$ ,  $T_p$ ,  $N_p$ ) and compute 6 statistical measures from them. The measures that serve as features for machine learning include the mean value, standard deviation, minimum and maximum values, the ratio between the maximum and minimum values, and the ratio between the mean value and standard deviation, also known as the coefficient of variation. These features are calculated for either the sheath region alone or the sheath region plus several hours of the magnetic obstacle interval (for example, using the first 4 hours into the magnetic obstacle, as illustrated before).

By computing feature values for all selected ICME events, we create a  $42 \times 348$  feature matrix with 14616 entries. We define two targets that we want to predict inside the magnetic obstacle: (1) the minimum of the  $B_z$  component,  $\min(B_z)$ ; and (2) the maximum of the total magnetic field,  $\max(B_t)$ .

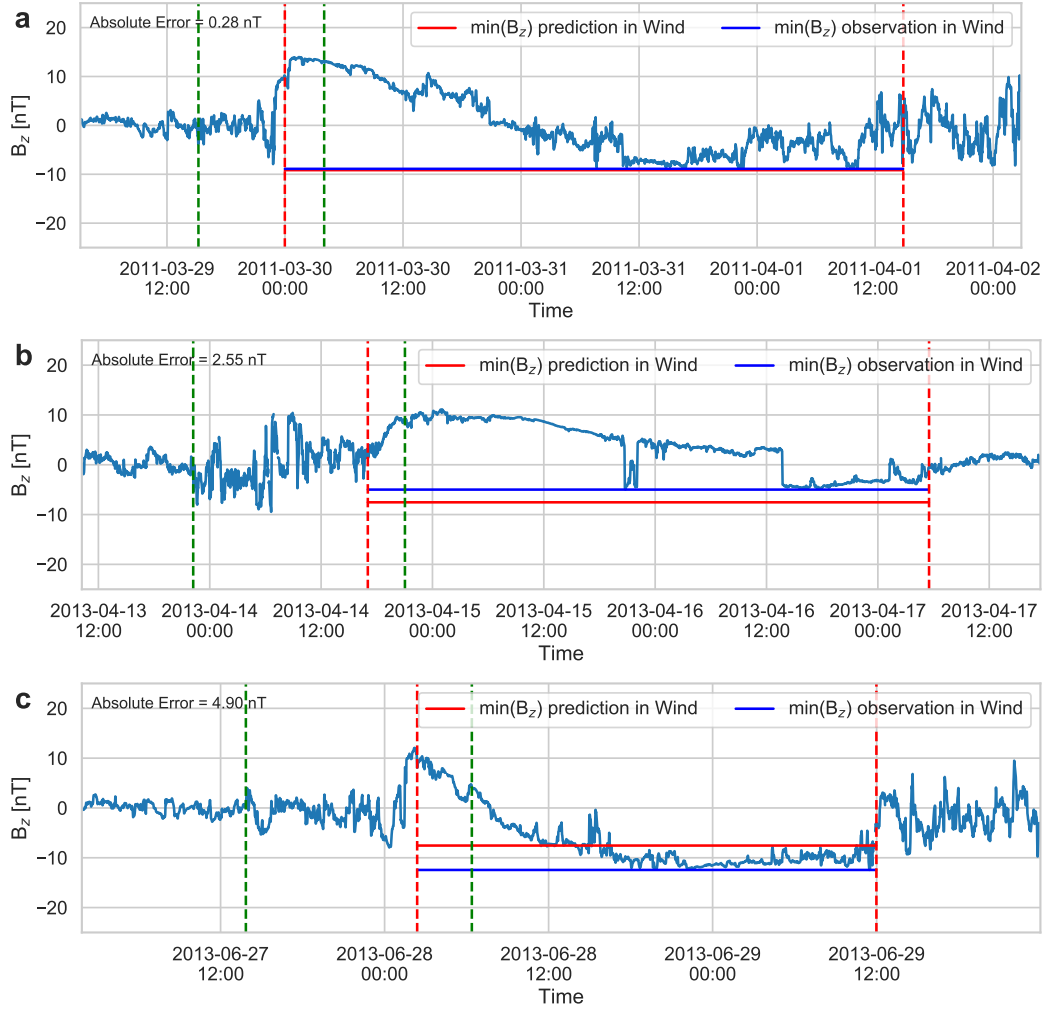


**Figure 3.** Comparison of the predicted minimum value of the  $B_z$  component in the magnetic obstacle using a Gradient Boosting Regressor (red) with the observation (blue). The absolute errors are close to the ideal prediction (a), median validation error (b), and the 75% percentile in the absolute error (c), respectively. The green dashed lines mark the time interval where we compute the feature values, and the red dashed lines mark the magnetic obstacle where we predict  $B_z$ . In this illustration, we use the ICME sheath and the first 4 hours of the magnetic obstacle for the  $B_z$  prediction.

### 3.2 Machine Learning Algorithms

We use a linear regressor (LR), random forest regressor (RFR), and gradient boosting regressor (GBR, see Friedman, 2001) from the widely-applied Python package Scikit-Learn to train a model. We select the RFR and the GBR from many learners because they provide the most accurate predictions for the problem at hand, are robust algorithms for training, and are efficient to implement and tune. The RFR and GBR both rely on an ensemble of decision trees that show powerful predictive skill when combined in a forest. We also provide the results from an LR that acts as a benchmark against which future versions of the predictive tool and studies can be easily compared.

### 3.3 Training and Testing

For every ICME, we have computed 6 statistical measures for 7 physical properties, resulting in a total of 42 features. We identify those features that affect the prediction the most. To validate the real-world performance, we split the input data into training and testing data. This final hold-out testing set is not used in training. By using the testing set for assessing the prediction, we attempt to extrapolate the model's skill to unseen behavior. The training set includes 243 ICMEs, and the testing set includes 105 ICMEs, randomly selected. This selection corresponds to 70% and 30% from all the events. During training, we further split the training data set into train and validation data, to which stratified 5-fold cross-validation and early stopping are applied to prevent over-fitting.

### 3.4 Hyperparameter Tuning

We perform hyperparameter tuning for the RFR and GBR for the selected set of features. To do so, we use a grid search and test combinations of parameter sets. We examine every point in the 4D (5D) parameter space within specified parameter ranges and use the parameter setting to train the GBR (RFR). Relying on the selected scoring measure, we use the best parameter setting for the training. After the grid search, we create a model including 200 decision trees (300), where the maximum depth of each tree is 3 (5) for the GBR (RFR). The minimum number of samples to define a node split or set a leaf was also defined in hyperparameter tuning for the RFR and GBR.

### 3.5 Experimental Real-Time Mode

We furthermore attempt to simulate an operational space weather forecast. To do so, we feed the features into the predictive tool as if an ICME sweeps over the spacecraft in an experimental real-time mode, resulting in a string of separately trained models for each input sheath duration that are applied in succession. We study how progressively adding features from the ICME sheath and the magnetic obstacle improves the  $B_z$  prediction. By doing so, we assess how many hours from the magnetic sheath and magnetic obstacle are required to achieve a certain accuracy in magnetic obstacle  $\max(B_t)$  and  $\min(B_z)$  predictions. Conducting such an experiment is useful because it allows estimating the reliability of the predictive tool in an operational situation, and furthermore points to possible weaknesses in the methodology.

## 4 Validation Analysis and Metrics

We assess the skill of the machine learning algorithms for predicting  $\min(B_z)$  and  $\max(B_t)$  with widely-applied validation metrics. These metrics are computed from a comparison between measurements and predictions in terms of continuous and binary variables. Contrary to continuous variables that can take on any real numbers, binary variables are categorical such as event and non-event predictions (see, for instance, Owens et al., 2005; Reiss et al., 2016; Wold et al., 2018). Focusing on both approaches, we com-

**Table 1.** Overview of point-to-point comparison metrics.

Metric	Short Name	Definition
Mean error	ME	$\frac{1}{n} \sum_{k=1}^n (f_k - o_k)$
Mean square error	MSE	$\frac{1}{n} \sum_{k=1}^n (f_k - o_k)^2$
Mean absolute error	MAE	$\frac{1}{n} \sum_{k=1}^n  f_k - o_k $
Root mean square error	RMSE	$\sqrt{\frac{1}{n} \sum_{k=1}^n (f_k - o_k)^2}$
Skill score	SS	$1 - \frac{\text{MSE}_{\text{pred}}}{\text{MSE}_{\text{ref}}}$

pute average errors from the comparison of the predicted and observed magnetic fields, and then investigate an event-based validation analysis.

#### 4.1 Point-to-point Metrics

First, we compare the predictions with observations in terms of statistical measures such as the mean, median, and standard deviation. These basic measures contain important information on the underlying statistical distribution of the predicted and observed values indicating, for example, if a model tends to over- or under-estimate the measurement.

In addition, we study the model accuracy in terms of error functions such as the mean error (ME), mean absolute error (MAE), and the root mean square error (RMSE). Table 1 summarizes these error functions, where  $(f_k, o_k)$  is the  $k$ -th element of  $n$  pairs of forecasts and observations. Although strictly speaking not an error function, we also include the Pearson correlation coefficient (PCC) in the analysis.

Next, we examine if our predictive tool is more useful than a simple baseline model. Baseline models are a valuable diagnostic to determine the skill of a novel model approach relative to a naive prediction. Baseline models in the space weather community often rely on the mean value of past observations (see, for example, Owens, 2018). For the sake of consistency, we define our baseline model as the mean value of all the targets we train our machine learning algorithms on.

In this context, the skill score (SS) is a measure that quantifies the skill of a forecast in comparison to the baseline model. Table 1 shows the definition of SS, where  $\text{MSE}_{\text{pred}}$  is the mean square error of the prediction, and  $\text{MSE}_{\text{ref}}$  is the MSE of the reference baseline model. A negative SS means the model is worse than the baseline model, a SS of 0 means the model is equal to the baseline model, whereas 1 indicates an ideal prediction.

#### 4.2 Binary Metrics

By categorizing each  $\min(B_z)$  and  $\max(B_t)$  prediction in terms of event/non-event predictions, we complement the analysis in the previous section. The advantages are plentiful as outlined in Owens (2018). First, error functions give equal importance to weak and strong magnetic field strength. Some users of our predictive tool, however, are only interested in the ability of forecasting events above a certain threshold, while smaller events are less important. Second, outliers in the prediction significantly affect point-to-point

**Table 2.** Overview of binary metrics defined by the entries of a contingency table.

Metric	Short Name	Definition
True Positive Rate	TPR	$\frac{TP}{TP+FN}$
False Positive Rate	FPR	$\frac{FP}{FP+TN}$
Threat Score	TS	$\frac{TP}{TP+FP+FN}$
True Skill Statistics	TSS	TPR – FPR
Bias	BS	$\frac{TP+FP}{TP+FN}$

comparison metrics. For users wanting to react when the event exceeds a defined threshold, an alternative is to consider each prediction as an event/non-event prediction.

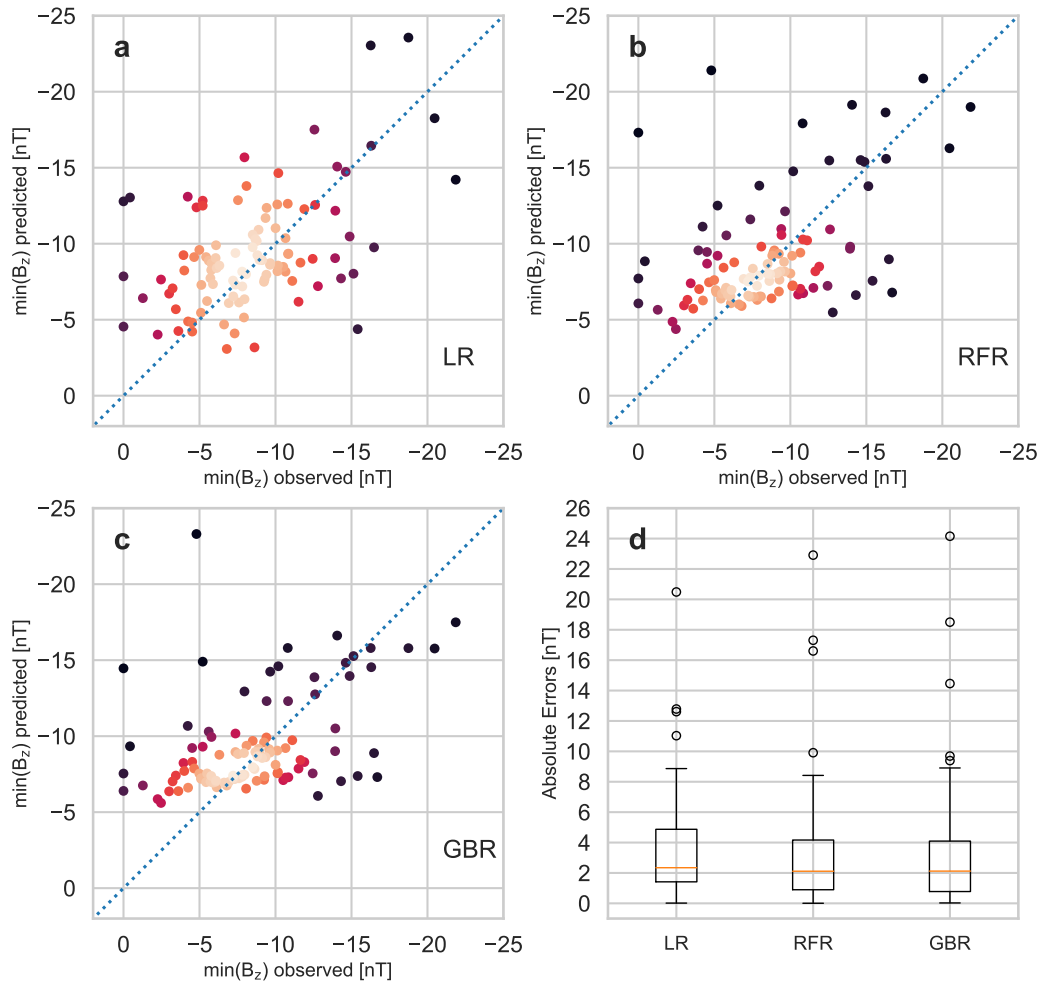
To define events and non-events in the observation and prediction, we use a threshold value equal to the mean value of all events in the ICME catalog. Through the cross-check of event and non-event combinations in the observed and predicted MFR properties, we count the number of hits (true positives; TPs), false alarms (false positives; FPs), misses (false negatives; FNs), and correct rejections (true negatives; TNs). Summarized in the so-called contingency table, a TP is a correctly predicted event, while an FN is an event that was not predicted. On the other hand, an FP is a predicted event that was not observed, and a TN is a correctly predicted non-event.

Table 2 shows skill measures that we compute from the entries of the contingency table. Here the ratio between the number of predictions and observations, also known as Bias (BS), shows the tendency of the GBR to over- or under-estimate the number of events. In addition, the true skill statistics (TSS) lies in the range  $[-1, 1]$ , where an ideal prediction would have the value 1 (or -1 for an optimum inverse prediction), and a TSS of 0 means no skill. One benefit of the TSS is that it uses all the elements in the contingency table and that it is unbiased by the proportion of predicted and observed events (see Hanssen & Kuipers, 1965; Bloomfield et al., 2012).

## 5 Results

We validate the predictive tool on data unused in our machine learning investigation, which is the test data set with 105 ICMEs. We then let each ICMEs sweep over the spacecraft in an experimental real-time mode and assess how additional information from several hours inside the magnetic flux rope improves the predictive skill.

To illustrate the skill of the predictive tool, we plot the prediction of the minimum value of the  $B_z$  component versus the observation. For this illustration, we feed data from the sheath region and 4 hours from the beginning of the magnetic obstacle into three machine learning algorithms. **Figure 4(a–c)** shows a comparison of the prediction and observation of  $\min(B_z)$  for the linear regressor (LR), random forest regressor (RFR), and the gradient boosting regressor (GBR), respectively. **Figure 4(d)** shows the boxplot for the absolute error of the different algorithms. Here the red line is the median error (50<sup>th</sup> percentile), the edges are the 25<sup>th</sup> and 75<sup>th</sup> percentiles, the whiskers show the  $\pm 2.5\sigma$  range covering 99.3% of the data, and the outliers are plotted as black circles. Agreement of the data points with the blue dashed lines in **Figure 4(a–c)** indicate the best performance. In comparison, the PCC for the LR, RFR, and GBR is 0.32, 0.70, and 0.71, re-



**Figure 4.** Comparison of the predicted and observed minimum value of the  $B_z$  component with three different machine learning algorithms, where the color scales with the density of the data points. (a) Linear Regressor; (b) Random Forest Regressor; (c) Gradient Boosting Regressor; (d) absolute error of the different algorithms. Data from the sheath region and the first 4 hours of the magnetic obstacle were used to train these models.

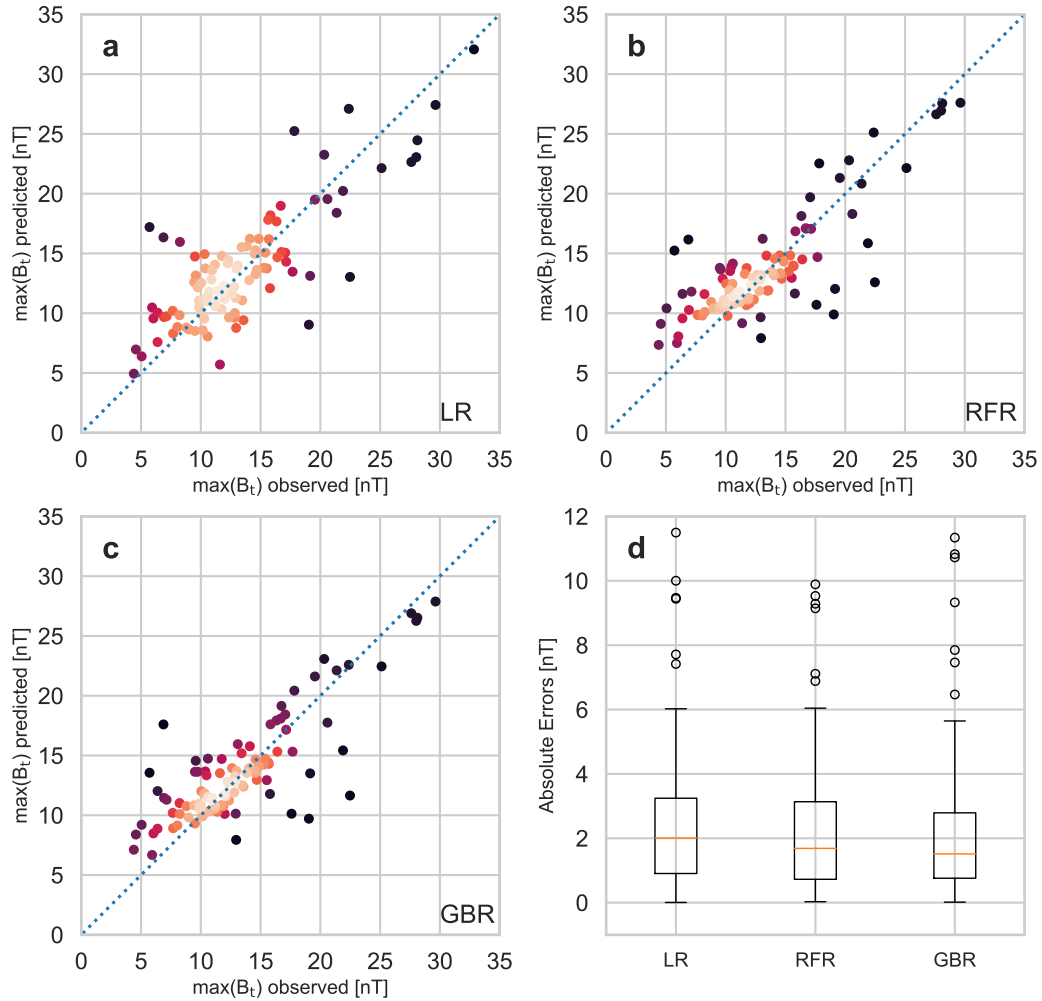


**Figure 5.** Comparison of the predicted and observed maximum value of the total magnetic field with three different machine learning algorithms, where the color scales with the density of the data points. (a) Linear Regressor; (b) Random Forest Regressor; (c) Gradient Boosting Regressor; (d) absolute error of the different algorithms. Data from the sheath region and the first 4 hours of the magnetic obstacle were used to train these models.

**Table 3.** Predictive abilities in terms of arithmetic mean (AM), standard deviation (SD), mean error (ME), mean absolute error (MAE), root mean square error (RMSE), the skill score (SS) relative to the simple mean value of all events, and the Pearson correlation coefficient (PCC). We use the sheath plus the first 4 hours of the MO to predict  $\min(B_z)$  and  $\max(B_t)$ , respectively.

Target	Model	AM [nT]	SD [nT]	ME [nT]	MAE [nT]	RMSE [nT]	SS	PCC
$\min(B_z)$	LR	-9.67	12.26	0.61	4.80	11.97	-2.24	0.32
$\min(B_z)$	RFR	-9.47	4.58	0.41	3.16	4.73	0.49	0.70
$\min(B_z)$	GBR	-9.58	4.12	0.52	3.12	4.77	0.49	0.71
$\min(B_z)$	Observation	-9.06	6.65	-	-	-	-	-
$\max(B_t)$	LR	14.18	11.15	-0.28	3.64	9.48	-0.55	0.54
$\max(B_t)$	RFR	14.09	5.68	-0.19	2.41	3.79	0.75	0.88
$\max(B_t)$	GBR	14.18	6.33	-0.29	2.23	3.20	0.82	0.91
$\max(B_t)$	Observation	13.89	7.63	-	-	-	-	-

spectively. While the LR, our benchmark model, is in poor agreement with the observations, more reasonable results are achieved for the RFR and GBR.

**Figure 5** shows the same illustration for the maximum value of the total magnetic field  $\max(B_t)$ . All three algorithms show considerably higher accuracy in comparison to the previous results. In particular, the PCC for the LR, RFR, and GBR is 0.54, 0.88, and 0.91, respectively. Both the RFR and GBR show promise for predicting  $\max(B_t)$  as an estimate of the  $B_z$  component.

For a more detailed error analysis, we compute point-to-point metrics as defined in **Table 1**. The first three rows in **Table 3** show the results of the different algorithms for  $\min(B_z)$ , and the columns show the corresponding values. The last row in the table shows the arithmetic mean (AM) and the standard deviation (SD) of the observation. From the results for  $\min(B_z)$ , we see that the RFR and GBR outperform the LR in all metrics. While the MAE for the RFR and GBR is 3.16 nT and 3.12 nT, the MAE for the LR is 4.80 nT. Also, the PCC for the RFR and GBR is 0.70 and 0.71, the PCC for the LR is 0.32. This trend is confirmed in the SS comparing the skill to a baseline model. We find that the LR is worse than the baseline model with negative SS, and the results for the RFR and GBR are 0.49, where 0 would indicate the same skill as the baseline, and 1 would indicate an optimum forecast.

The last three rows in **Table 3** show the results of the different machine learning models for predicting  $\max(B_t)$ . Again we find that the RFR and GBR outperform the LR. For example, the MAE for the RFR and GBR is 2.41 nT and 2.23 nT, the MAE for the LR is 3.64 nT. Focusing on the differences between the RFR and GBR for both targets, we find that both perform similarly, with GBR providing slightly better predictions.

We furthermore investigate an operational setting where an ICME sweeps over the spacecraft. In this experimental real-time mode, we quantify how additional information from the magnetic flux rope improves the skill of the machine learning algorithms. **Figure 6** shows the skill of a string of trained RFR and the GBR models for the prediction of  $\min(B_z)$  and  $\max(B_t)$ . The first data point at 0 hours always denotes the start of the magnetic obstacle where features are computed only from the sheath region. With increasing time elapsed from the magnetic obstacle start, more information from the target is included in the input data. As expected, we find that increasing the information from the magnetic obstacle improves the accuracy of the predictive skill. As an example, the PCC for the  $\min(B_z)$  RFR prediction and  $\max(B_t)$  RFR prediction improves

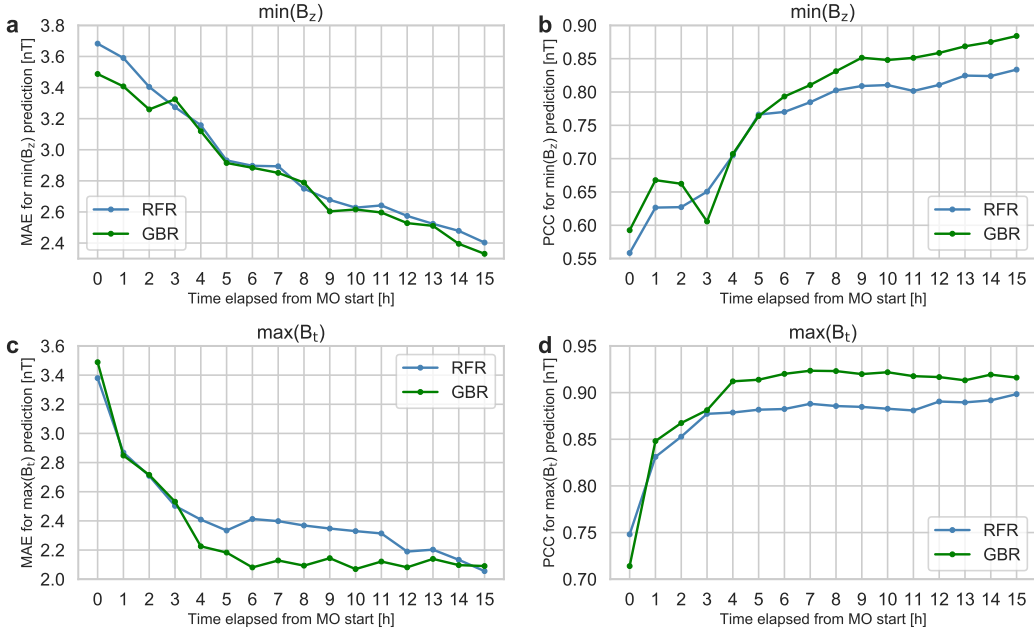


**Figure 6.** Effect of the time elapsed from the magnetic obstacle start on the predictive ability of the different machine learning models. (a) MAE for the  $\min(B_z)$  prediction; (b) PCC for the  $\min(B_z)$  prediction; (c) MAE for the  $\max(B_t)$  prediction; (d) PCC for the  $\max(B_t)$  prediction.

in the first 4 hours by approximately 14% and 13%. We also find that more data from the magnetic obstacle improves the LR predictions (not shown in the plot). However, the variations in the LR predictions are significantly larger in comparison to the RFR and GBR when seeing more from the magnetic obstacle.

We complement this analysis with an event-based validation study. We specifically use the mean value of the observation as an event threshold. Values below a threshold of  $-9.06$  nT for  $\min(B_z)$  and above  $13.89$  nT for  $\max(B_t)$  signify an event, and all other values are not events. As discussed in **Section 3.2**, the results of this analysis can be summarized in a contingency table, from which we can compute the measures defined in **Table 2**. **Table 4** lists the resulting measures for the different learners. In terms of an actionable prediction, the RFR provides the best results with a TSS of 0.30, followed by the GBR with a TSS of 0.28, and the LR with a TSS of 0.18. Again we find a clear gap between the LR and the other two models. These differences indicate that the results by the LR are not only less promising in predicting the exact values but also in predicting the severity of the ICME.

In quantitative measures, we find that the GBR was able to predict if  $\min(B_z)$  is below  $-9.06$  nT in 77% of all observed ICMEs in this category. On the other hand, 47% of all the events above  $-9.06$  nT were erroneously classified as being below this threshold by the GBR. When focusing on  $\max(B_t)$  as an approximation, the results are significantly better. More specifically, the GBR was able to predict if  $\max(B_t)$  is above  $13.89$  nT in 77% of all observed ICMEs in this category, and only 11% of all the events below  $13.89$  nT were erroneously classified.

In essence, we find that the RFR and GBR at the heart of the predictive tool provide some promising first results and justify their use. While not solving the  $B_z$  problem, this prototype of a predictive tool can narrow down the extent of the  $B_z$  component expected during the ICME arrival at Earth. We find that the predictive ability of

**Table 4.** Contingency table and skill measures for an event-based validation analysis. The table shows the number of observed ( $N_{\text{obs}}$ ) and predicted ( $N_{\text{pred}}$ ) events, hits (true positives; TPs), false alarms (false positives; FPs), misses (false negatives, FNs), correct rejections (true negatives, TNs), and the metrics derived from these entries including: the true positive rate (TPR) and false positive rate (FPR), threat score (TS), true skill statistics (TSS), and bias (BS).

Target	Model	$N_{\text{obs}}$	$N_{\text{pred}}$	TP	FP	FN	TN	TPR	FPR	TS	TSS	BS
$\min(B_z)$	LR	60	60	39	21	21	24	0.65	0.47	0.48	0.18	1.00
$\min(B_z)$	RFR	60	67	46	21	14	24	0.77	0.47	0.57	0.30	1.12
$\min(B_z)$	GBR	60	68	46	22	14	23	0.77	0.49	0.56	0.28	1.13
$\max(B_t)$	LR	39	41	28	13	11	53	0.72	0.20	0.54	0.52	1.05
$\max(B_t)$	RFR	39	34	28	6	11	60	0.72	0.09	0.62	0.63	0.87
$\max(B_t)$	GBR	39	37	30	7	9	59	0.77	0.11	0.65	0.66	0.95

the tool increases considerably with additional information as an ICME sweeps over the spacecraft.

## 6 Automated ICME Detection

Any scenario to apply the predictive tool in operational space weather forecasting needs a reliable automated ICME detection functionality. In the following, we present our implementation of the detection algorithm as introduced in Nguyen et al. (2019) and compare the detected ICMEs with events from the ICMECATv2.0 catalog.

### 6.1 Automated Detection Algorithm

Our implementation to detect the start of the ICME sheath region in Wind, STEREO-A, and STEREO-B mission relies on the algorithm developed in Nguyen et al. (2019). The authors tested the algorithm with in situ measurements from the Wind spacecraft between the years 1997 and 2015 with promising results. They found a maximum precision of  $84\% \pm 2.6\%$  and a recall of  $84\% \pm 4.5\%$ . In other words, approximately 84% of all the identified events were ICMEs, and approximately 84% of all the observed ICMEs were correctly identified.

The automated detection algorithm uses a sliding window approach combined with a convolutional neural network to predict the likelihood that the window under scrutiny features an ICME event. We specifically move windows with a duration of 1 to 29 hours over the in situ measurements from the three different spacecraft. To evaluate the likelihood that a sliding window includes an ICME, we train a convolutional neural network to predict a measure known as similarity. The similarity ( $s$ ) of window  $X_i$  and event $_j$  is defined by

$$s(X_i, \text{event}_j) = \frac{\text{duration}(X_i \cap \text{event}_j)}{\text{duration}(X_i \cup \text{event}_j)}, \quad (1)$$

where  $s$  is equal to 0 if there is no ICME in the window and close to 1 if there is an ICME from the catalog in the window.

To predict  $s$  from a convolutional neural network, we use the physical properties in Section 2 and add the plasma  $\beta$ , dynamic pressure ( $P_{\text{dyn}}$ ), ratio of proton temperature to the expected proton temperature ( $T_p/T_{\text{ex}}$ ), and the rolling standard deviation, which results in 11 features. We scale and normalize these features to have an average of 0 and a standard deviation of 1.

**Table 5.** Time intervals for training, validating and testing the automated ICME detection for the Wind, STEREO-A, and STEREO-B spacecraft.

Spacecraft	Validation Set [years]	Training Set [years]	Test Set [years]
Wind	2007	2008 to 2018	2019 to 2021
STEREO-A	2007	2008 to 2018	2019
STEREO-B	2007	2008 to 2012	2013 to 2014

**Table 6.** Contingency table entries and mean time error for the automated ICME detection algorithm. The table shows the spacecraft, number of observed ( $N_{\text{obs}}$ ) and predicted ( $N_{\text{pred}}$ ) events, hits (true positives; TPs), false alarms (false positives; FPs), misses (false negatives; FNs) and the mean time error given in percent of the sheath duration.

Spacecraft	$N_{\text{obs}}$	$N_{\text{pred}}$	TP	FP	FN	Mean Time Error [% of sheath duration]
WIND	11	59	10	49	1	51.6
STEREO-A	11	36	8	28	3	36.9
STEREO-B	24	75	18	57	6	9.6

We then use these features to train a neural network to predict  $s$  at any time for the three spacecraft. Table 5 shows the time intervals for training, validating, and testing the neural network. To convert the predicted similarity timeline to a list of events, we integrate  $s$  over the different window sizes and use a multiple-Gaussian fit for regularization. Finally, we use a peak detection algorithm when the integral exceeds a manually defined decision threshold. For a more detailed description of the detection algorithm, we refer the reader to Nguyen et al. (2019).

## 6.2 Validation Analysis

To assess the accuracy of the automated ICME detection, we compare the automatically detected ICMEs to the events in the ICMECATv2.0 catalog. By cross-checking detected and observed ICMEs, we count the number of hits (true positives, TPs), false alarms (false positives, FPs), and misses (false negatives, FNs). We label a detected event as a hit if the overlap is at least 10%.

**Table 6** shows the results of the automated ICME detection in terms of an event-based analysis. We find that the automated detection algorithm can detect almost all the ICMEs included in the catalog. These hits, however, only come with a significant number of false alarms. Adding the results for the different spacecraft, we find that 76.1 percent of all the ICMEs in the catalog were correctly detected, but only 20.7 percent of all the predictions were correct. We additionally obtain a mean time error between the predicted and observed event start of 51.6%, 36.9%, and 10.4% of the sheath region for the Wind, STEREO-A, and STEREO-B spacecraft, respectively.

We complement this analysis by focusing on binary event metrics where each point in time is labeled as an event or non-event. In this context, the receiver operator characteristic (ROC) curve illustrates the predictive capabilities for a range of different event thresholds. Figure 7(a) shows how the number of correctly predicted events (TPR) varies with the number of incorrectly predicted non-events (FPR). A perfect classification is indicated by a TPR of 1 and an FPR of 0, summarized by an area under the curve (AUC) of 1.

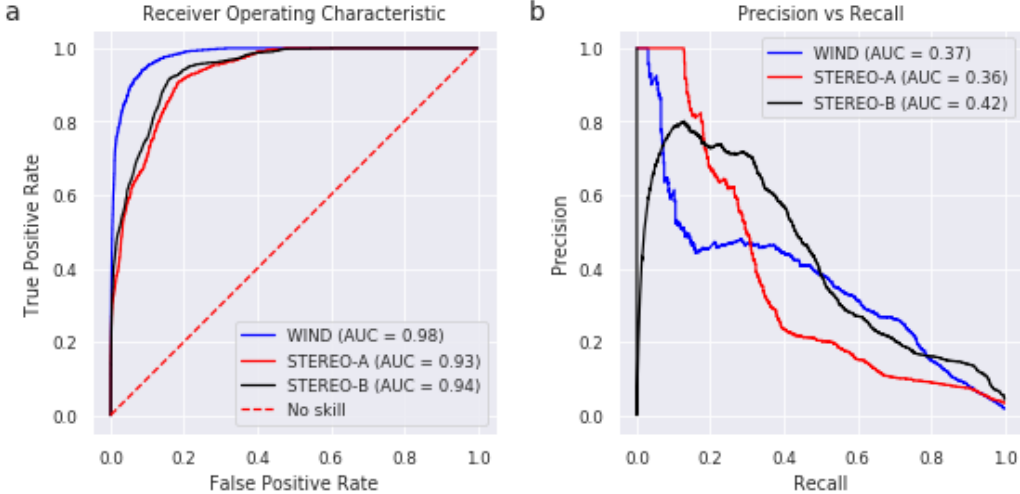


**Figure 7.** Event-based validation of the automated ICME detection algorithm showing (a) the ROC and (b) the Precision-Recall curve for Wind, STEREO-A, and STEREO-B mission data.

An inherent problem we need to consider is the low number of observed ICMEs. This data imbalance means that even an algorithm classifying each time step as non-event would produce a convincing ROC curve. To better account for that, we focus on the relationship between precision and recall. While the recall is equivalent to the TPR, precision is the fraction of correctly predicted events among all the predicted events. Figure 7(b) shows how correctly predicted events among all the predicted events (precision) varies with the correctly predicted events among all the observed events (recall). We find that the precision of the automated detection significantly decreases with increasing recall. This trend indicates that the more ICMEs from the catalog are correctly detected, the larger the number of false alarms.

We conclude that further developments of this prototype are needed to succeed with an operational  $B_z$  prediction tool. Although the automated ICME detection algorithm shows first glimpses of success, more research is required to reduce the number of false alarms in our algorithm implementation.

## 7 Discussion

A traditional way of approaching the  $B_z$  problem is to simulate the propagation of ICMEs with MHD codes. Examples are SUSANOO-CME (Shiota & Kataoka, 2016), AWSOM-SWMF (Jin et al., 2017), MAS (Török et al., 2018), and EUHFORIA (Poedts et al., 2020). These MHD codes include the magnetic flux rope structure and simulate the ICME evolution from near the Sun into interplanetary space. Although a full physics-based description is desirable, a breakthrough in solving the  $B_z$  problem with MHD codes alone is challenging. On the one hand, the boundary conditions for all MHD codes are based on solar magnetic field measurements, but these are known to have large inherent uncertainties. Additionally, small uncertainties in the initial conditions of a CME grow to large errors in the predicted magnetic field components at 1 AU (Kay & Gopalswamy, 2018; Möstl et al., 2018). Even with flux-transport models based on Sun-Earth line observations, it is difficult to develop a time-dependent coronal magnetic model, which is needed to capture the early CME evolution. On the other hand, the solar corona is not strictly an MHD environment. While an MHD simulation can describe the large-scale coronal conditions within the Alfvén surface, the evolution of CMEs occurs over a broad

range of spatial scales. Small-scale processes such as triggering instabilities are essential to capture the whole picture. Without a definitive physical solution, we need to study new predictive tools that can enhance  $B_z$  prediction capabilities, and ideally, provide constraints for physics-based models.

In this context, we have studied the hypothesis that upstream in situ measurements of the sheath region and the first few hours of the magnetic flux rope of the ICME are useful to predict estimates of the  $B_z$  component. To test this hypothesis, we developed a predictive tool based on machine learning that is trained and tested on 348 ICMEs. We found that the tool can predict the minimum value of the  $B_z$  component (PCC= 0.71) and the maximum value of the total magnetic field  $B_t$  (PCC= 0.91) in the magnetic obstacle in reasonable agreement with observations. While the investigated hypothesis certainly does not solve the  $B_z$  problem, it shows promising first results for ICMEs that have a magnetic flux rope signature, and its application might be useful for operational space weather forecasting.

To put our results into context, we want to discuss the following three limitations of our study. First, we have significantly reduced the complexity of the  $B_z$  problem by focusing on estimates of the  $B_z$  component for the whole magnetic flux rope, specifically  $\min(B_z)$  and  $\max(B_t)$ . Focusing on these large-scale statistics of the magnetic flux rope is considerably easier than predicting the temporal evolution of  $B_z$ . Nevertheless, the ability of our prototype to predict  $\min(B_z)$ , a proxy for ICME geoeffectiveness, is essential in an actionable forecast.

Second, we have trained and tested the machine learning algorithms on ICMEs that occurred between the years 2007 to 2021 using the ICMECATv2.0 catalog. The main criterion was that the ICMEs needed to show either sheath region signatures or a density pileup in front of a magnetic obstacle. This criterion reduced the number of ICMEs to approximately 65% of the original catalog. The expected magnetic flux rope signatures in this study include increasing magnetic field strength, rotation of at least one field component, and plasma- $\beta < 1$  (L. F. Burlaga, 1988). These signatures are not always observed by satellites (Rouillard et al., 2009; Wood & Howard, 2009; Vourlidas, 2014). We know that flux ropes undergo deformation and distortion during their dynamic evolution, often leading to significant deviation from an idealized flux rope structure (Riley et al., 2006; Savani et al., 2010; Nieves-Chinchilla et al., 2012). Therefore, an open question is how well we can extrapolate the predictive skill presented here to an operational space weather forecast.

Third and in the context of the last point, we know that the success of the predictive tool in any operational setting will depend on accurate automated ICME detection in mission data as introduced in Telloni et al. (2019); Nguyen et al. (2019). Although we have shown that the coupling of our approach with an automated ICME detection algorithm shows promise, such a combined framework introduces new challenges. For example, we need to reduce the number of false alarms. Beyond that, we need to understand better the effect of a timing error in the automated ICME detection on the coupled predictive tool for the  $B_z$  prediction. More research is needed to assess these uncertainties and understand their effect on the robustness and reliability of the  $B_z$  prediction.

In the future, we will work on several topics to improve upon this prototype. Besides improving the coupling of our predictive tool and the automated ICME detection algorithm, we will also work on new strategies to forecast the temporal evolution of the  $B_z$  component. Here, our approach is two-fold. Initially, a data driven machine learning approach to predict the temporal evolution of the  $B_z$  component is envisaged. Next, we will explore the integration of a semi-empirical magnetic flux rope model as discussed in Weiss, Möstl, Amerstorfer, et al. (2021) and Weiss, Möstl, Davies, et al. (2021) in our framework. The advantage of this technique is that it can model the CME flux ropes in

conjunction with an approximate Bayesian computation (ABC) algorithm that fits the model to in situ magnetic field measurements. We will study if the model can fit the rest of the magnetic flux rope from the first few hours of the ICME. For both approaches, we aim to deduce error boundaries for the  $B_z$  prediction.

In a long-term vision, our predictive tool could make use of mission data from a space weather monitor closer to the Sun using solar sail technology (West, 2004). When the space weather monitor is placed near the Sun-Earth line at approximately  $3 \times 10^6$  km upstream from Earth or twice the distance to L1, the warning time compared to L1 satellites is doubled. In other words, for an ICME traveling with 400 km/s (which is close to the median speed of the ICMEs under scrutiny), the lead time before the event arrives at Earth increases from approximately 1 hour to 2 hours. Since the present methodology is developed and tested for three different spacecraft, our predictive tool could be easily expanded to future space missions.

To allow the community to compare future studies with our findings, the source code, ICMECATv2.0 catalog, and related data are available online as outlined in Section 9.

## 8 Summary

The capacity of ICMEs to cause extreme geomagnetic storms fundamentally depends on their internal plasma structure and their  $B_z$  magnetic field. At present, we can not predict the  $B_z$  magnetic field component with sufficient warning time before the ICME arrival at Earth. This conundrum is often called the  $B_z$  problem.

We shine new light on the  $B_z$  problem by studying the research question if upstream in situ measurements of the ICME sheath region and the first few hours of the magnetic flux rope are sufficient for predicting the  $B_z$  component. To do so, we developed a predictive tool based on machine learning that is trained and tested on 348 ICME events observed by the Wind, STEREO-A, and STEREO-B spacecraft. We train machine learning models to output the minimum value of the  $B_z$  component and the maximum value of the total magnetic field  $B_t$  in the magnetic obstacle.

To test our predictive tool in an experimental real-time mode, we let the ICMEs sweep over the spacecraft and assess how continually feeding new information into the tool improves the  $B_z$  predictions. Since the operational use of the tool needs a reliable detection of ICMEs in mission data, we then implement an existing automated ICME detection algorithm and test its reliability for the ICMEs under scrutiny.

Our study shows that the predictive tool can predict the minimum value of the  $B_z$  component (MAE= 3.12 nT, PCC= 0.71) and the maximum value of the total magnetic field  $B_t$  (MAE= 2.23 nT, PCC= 0.91) in the magnetic obstacle in reasonable agreement with observations. While the investigated hypothesis does not solve the  $B_z$  problem, the first version of the predictive tool shows reasonable results for ICMEs that have a clear magnetic flux rope signature, and its application might be suited for operational space weather forecasting in the future.

## 9 Data Availability Statement

The solar wind in situ data are available as python numpy arrays at <https://doi.org/10.6084/m9.figshare.12058065.v8> (updated on 2021 April 29) and were originally downloaded from <https://stereo-ssc.nascom.nasa.gov> (STEREO) and <https://spdf.gsfc.nasa.gov/pub/data/wind/> (Wind). The current version of the ICME catalog ICMECATv2.0, version 6 updated on 2021 April 29 and as published on the data sharing platform figshare, was used in this study: <https://doi.org/10.6084/m9.figshare.6356420.v6>. (The most up-to-date version can be found at <https://helioforecast.space/>

icmecat.) The paper source code is available at [https://github.com/helioforecast/Papers/tree/master/Reiss2021\\_MLrope](https://github.com/helioforecast/Papers/tree/master/Reiss2021_MLrope).

### Acknowledgments

M.A.R., C.M., R.L.B., U.V.A., T.A., A.J.W., and J.H. thank the Austrian Science Fund (FWF): P31659-N27, P31521-N27, and P31265-N27. Europlanet 2024 RI has received funding from the European Union's Horizon 2020 research and innovation programme under grant agreement No 871149.

### References

Bloomfield, D. S., Higgins, P. A., McAteer, R. T. J., & Gallagher, P. T. (2012, Mar). Toward reliable benchmarking of solar flare forecasting methods. *The Astrophysical Journal Letters*, 747(2), L41.

Bothmer, V., & Schwenn, R. (1998, January). The structure and origin of magnetic clouds in the solar wind. *Annales Geophysicae*, 16, 1-24. doi: 10.1007/s00585-997-0001-x

Burlaga, L., Sittler, E., Mariani, F., & Schwenn, R. (1981, August). Magnetic loop behind an interplanetary shock: Voyager, Helios, and IMP 8 observations. *J. Geophys. Res.*, 86(A8), 6673-6684. doi: 10.1029/JA086iA08p06673

Burlaga, L. F. (1988, July). Magnetic clouds and force-free fields with constant al- pha. *J. Geophys. Res.*, 93, 7217-7224. doi: 10.1029/JA093iA07p07217

Chen, J. (1996, December). Theory of prominence eruption and propaga- tion: Interplanetary consequences. *Journal of Geophysical Research: Space Physics*, 101(A12), 27499-27519. Retrieved 2016-07-14, from <http://onlinelibrary.wiley.com/doi/10.1029/96JA02644/abstract> doi: 10.1029/96JA02644

Chen, J., Cargill, P. J., & Palmadesso, P. J. (1997, July). Predicting solar wind structures and their geoeffectiveness. *J. Geophys. Res.*, 102(A7), 14701-14720. doi: 10.1029/97JA00936

dos Santos, L. F. G., Narock, A., Nieves-Chinchilla, T., Nuñez, M., & Kirk, M. (2020, October). Identifying Flux Rope Signatures Using a Deep Neural Net- work. *Sol. Phys.*, 295(10), 131. doi: 10.1007/s11207-020-01697-x

Dungey, J. W. (1961, January). Interplanetary Magnetic Field and the Auroral Zones. *Phys. Rev. Lett.*, 6, 47-48. doi: 10.1103/PhysRevLett.6.47

Echer, E., Gonzalez, W. D., Tsurutani, B. T., & Gonzalez, A. L. C. (2008, May). Interplanetary conditions causing intense geomagnetic storms (Dst  $\approx$  -100 nT) during solar cycle 23 (1996-2006). *Journal of Geophysical Research (Space Physics)*, 113(A5), A05221. doi: 10.1029/2007JA012744

Friedman, J. H. (2001). Greedy function approximation: A gradient boosting ma- chine. *The Annals of Statistics*, 29(5), 1189–1232.

Galvin, A. B., Kistler, L. M., Popecki, M. A., Farrugia, C. J., Simunac, K. D. C., El- lis, L., ... Steinfeld, D. (2008). The plasma and suprathermal ion composition (plastic) investigation on the stereo observatories. In C. T. Russell (Ed.), (pp. 437–486). New York, NY: Springer New York.

Gonzalez, W. D., & Tsurutani, B. T. (1987, September). Criteria of interplane- tary parameters causing intense magnetic storms (Dst of less than -100 nT). *Planet. Space Sci.*, 35, 1101-1109. doi: 10.1016/0032-0633(87)90015-8

Hanssen, A., & Kuipers, W. (1965). *On the relationship between the fre- quency of rain and various meteorological parameters: (with reference to the problem of objective forecasting)*. Staatsdrukerij. Retrieved from <https://books.google.at/books?id=nTZ80gAACAAJ>

Jin, M., Manchester, W. B., van der Holst, B., Sokolov, I., Tóth, G., Mullinix, R. E., ... Gombosi, T. I. (2017, January). Data-constrained Coronal Mass Ejec-

tions in a Global Magnetohydrodynamics Model. *ApJ*, *834*(2), 173. doi: 10.3847/1538-4357/834/2/173

Kay, C., & Gopalswamy, N. (2018, September). The Effects of Uncertainty in Initial CME Input Parameters on Deflection, Rotation,  $B_z$ , and Arrival Time Predictions. *Journal of Geophysical Research (Space Physics)*, *123*(9), 7220-7240. doi: 10.1029/2018JA025780

Kilpua, E. K. J., Balogh, A., von Steiger, R., & Liu, Y. D. (2017, Nov). Geo-effective Properties of Solar Transients and Stream Interaction Regions. *Space Sci. Rev.*, *212*, 1271-1314. doi: 10.1007/s11214-017-0411-3

Kim, R. S., Moon, Y. J., Gopalswamy, N., Park, Y. D., & Kim, Y. H. (2014, April). Two-step forecast of geomagnetic storm using coronal mass ejection and solar wind condition. *Space Weather*, *12*(4), 246-256. doi: 10.1002/2014SW001033

Lepping, R. P., Acuña, M. H., Burlaga, L. F., Farrell, W. M., Slavin, J. A., Schatten, K. H., ... Worley, E. M. (1995, February). The Wind Magnetic Field Investigation. *Space Sci. Rev.*, *71*, 207-229. doi: 10.1007/BF00751330

Luhmann, J. G., Curtis, D. W., Schroeder, P., McCauley, J., Lin, R. P., Larson, D. E., ... Gosling, J. T. (2008, April). STEREO IMPACT Investigation Goals, Measurements, and Data Products Overview. *Space Sci. Rev.*, *136*, 117-184. doi: 10.1007/s11214-007-9170-x

Möstl, C., Amerstorfer, T., Palmerio, E., Isavnin, A., Farrugia, C. J., Lowder, C., ... Boakes, P. D. (2018, Mar). Forward Modeling of Coronal Mass Ejection Flux Ropes in the Inner Heliosphere with 3DCORE. *Space Weather*, *16*(3), 216-229. doi: 10.1002/2017SW001735

Möstl, C., Isavnin, A., Boakes, P. D., Kilpua, E. K. J., Davies, J. A., Harrison, R. A., ... Zhang, T. L. (2017). Modeling observations of solar coronal mass ejections with heliospheric imagers verified with the heliophysics system observatory. *Space Weather*, *15*(7), 955-970.

Möstl, C., Weiss, A. J., Bailey, R. L., Reiss, M. A., Amerstorfer, T., Hinterreiter, J., ... Stansby, D. (2020, November). Prediction of the In Situ Coronal Mass Ejection Rate for Solar Cycle 25: Implications for Parker Solar Probe In Situ Observations. *ApJ*, *903*(2), 92. doi: 10.3847/1538-4357/abb9a1

Mulligan, T., Russell, C. T., & Luhmann, J. G. (1998). Solar cycle evolution of the structure of magnetic clouds in the inner heliosphere. *Geophys. Res. Lett.*, *25*, 2959-2962. doi: 10.1029/98GL01302

Nguyen, G., Aunai, N., Fontaine, D., Le Pennec, E., Van den Bossche, J., Jeandet, A., ... Regaldo-Saint Blanchard, B. (2019, April). Automatic Detection of Interplanetary Coronal Mass Ejections from In Situ Data: A Deep Learning Approach. *ApJ*, *874*(2), 145. doi: 10.3847/1538-4357/ab0d24

Nieves-Chinchilla, T., Colaninno, R., Vourlidas, A., Szabo, A., Lepping, R. P., Boardsen, S. A., ... Korth, H. (2012, June). Remote and in situ observations of an unusual Earth-directed coronal mass ejection from multiple viewpoints. *Journal of Geophysical Research (Space Physics)*, *117*(A6), A06106. doi: 10.1029/2011JA017243

Nieves-Chinchilla, T., Linton, M. G., Hidalgo, M. A., & Vourlidas, A. (2018, Jul). Elliptic-cylindrical Analytical Flux Rope Model for Magnetic Clouds. *ApJ*, *861*(2), 139. doi: 10.3847/1538-4357/aac951

Ogilvie, K. W., Chornay, D. J., Fritzenreiter, R. J., Hunsaker, F., Keller, J., Lobel, J., ... Gergin, E. (1995, February). SWE, A Comprehensive Plasma Instrument for the Wind Spacecraft. *Space Sci. Rev.*, *71*, 55-77. doi: 10.1007/BF00751326

Owens, M. J. (2018, November). Time-Window Approaches to Space-Weather Forecast Metrics: A Solar Wind Case Study. *Space Weather*, *16*(11), 1847-1861. doi: 10.1029/2018SW002059

Owens, M. J., Arge, C. N., Spence, H. E., & Pembroke, A. (2005). An event-based approach to validating solar wind speed predictions: High-speed enhance-

ments in the wang-sheeley-arge model. *Journal of Geophysical Research: Space Physics*, 110(A12), n/a–n/a. (A12105) doi: 10.1029/2005JA011343

Owens, M. J., & Forsyth, R. J. (2013, December). The Heliospheric Magnetic Field. *Living Reviews in Solar Physics*, 10(1), 5. doi: 10.12942/lrsp-2013-5

Owens, M. J., Lockwood, M., & Barnard, L. A. (2017, June). Coronal mass ejections are not coherent magnetohydrodynamic structures. *Nature Scientific Reports*, 7, 4152. doi: 10.1038/s41598-017-04546-3

Poedts, S., Lani, A., Scolini, C., Verbeke, C., Wijsen, N., Lapenta, G., ... Depauw, J. (2020, September). EUropean Heliospheric FORecasting Information Asset 2.0. *Journal of Space Weather and Space Climate*, 10, 57. doi: 10.1051/swsc/2020055

Reiss, M. A., Temmer, M., Veronig, A. M., Nikolic, L., Vennerstrom, S., Schoen-gassner, F., & Hofmeister, S. J. (2016, July). Verification of high-speed solar wind stream forecasts using operational solar wind models. *Space Weather*, 14(7), 2016SW001390. doi: 10.1002/2016SW001390

Riley, P., Ben-Nun, M., Linker, J. A., Owens, M. J., & Horbury, T. S. (2017, March). Forecasting the properties of the solar wind using simple pattern recognition. *Space Weather*, 15(3), 526–540. doi: 10.1002/2016SW001589

Riley, P., Schatzman, C., Cane, H. V., Richardson, I. G., & Gopalswamy, N. (2006, August). On the Rates of Coronal Mass Ejections: Remote Solar and In Situ Observations. *ApJ*, 647(1), 648–653. doi: 10.1086/505383

Rouillard, A. P. (2011, June). Relating white light and in situ observations of coronal mass ejections: A review. *Journal of Atmospheric and Solar-Terrestrial Physics*, 73(10), 1201–1213. doi: 10.1016/j.jastp.2010.08.015

Rouillard, A. P., Davies, J. A., Forsyth, R. J., Savani, N. P., Sheeley, N. R., Thernisien, A., ... Carr, C. M. (2009, Jul). A solar storm observed from the Sun to Venus using the STEREO, Venus Express, and MESSENGER spacecraft. *J. Geophys. Res.*, 114(A7), A07106. doi: 10.1029/2008JA014034

Salman, T. M., Lugaz, N., Farrugia, C. J., Winslow, R. M., Galvin, A. B., & Schwadron, N. A. (2018, December). Forecasting Periods of Strong Southward Magnetic Field Following Interplanetary Shocks. *Space Weather*, 16(12), 2004–2021. doi: 10.1029/2018SW002056

Savani, N. P., Owens, M. J., Rouillard, A. P., Forsyth, R. J., & Davies, J. A. (2010, May). Observational Evidence of a Coronal Mass Ejection Distortion Directly Attributable to a Structured Solar Wind. *ApJ*, 714, L128–L132. doi: 10.1088/2041-8205/714/1/L128

Savani, N. P., Vourlidas, A., Szabo, A., Mays, M. L., Richardson, I. G., Thompson, B. J., ... Nieves-Chinchilla, T. (2015, June). Predicting the magnetic vectors within coronal mass ejections arriving at Earth: 1. Initial architecture. *Space Weather*, 13, 374–385. doi: 10.1002/2015SW001171

Shiota, D., & Kataoka, R. (2016, February). Magnetohydrodynamic simulation of interplanetary propagation of multiple coronal mass ejections with internal magnetic flux rope (SUSANOO-CME). *Space Weather*, 14, 56–75. doi: 10.1002/2015SW001308

Telloni, D., Antonucci, E., Bemporad, A., Bianchi, T., Bruno, R., Fineschi, S., ... Susino, R. (2019, November). Detection of Coronal Mass Ejections at L1 and Forecast of Their Geoeffectiveness. *ApJ*, 885(2), 120. doi: 10.3847/1538-4357/ab48e9

Török, T., Downs, C., Linker, J. A., Lionello, R., Titov, V. S., Mikić, Z., ... Wijaya, J. (2018, Mar). Sun-to-Earth MHD Simulation of the 2000 July 14 “Bastille Day” Eruption. *ApJ*, 856, 75. doi: 10.3847/1538-4357/aab36d

Tsurutani, B. T., Gonzalez, W. D., Gonzalez, A. L. C., Guarneri, F. L., Gopalswamy, N., Grande, M., ... Vasyliunas, V. (2006, July). Corotating solar wind streams and recurrent geomagnetic activity: A review. *Journal of Geophysical Research (Space Physics)*, 111, A07S01. doi: 10.1029/2005JA011273

Vourlidas, A. (2014, June). The flux rope nature of coronal mass ejections. *Plasma Physics and Controlled Fusion*, *56*(6), 064001. doi: 10.1088/0741-3335/56/6/064001

Vourlidas, A., Lynch, B. J., Howard, R. A., & Li, Y. (2013, May). How Many CMEs Have Flux Ropes? Deciphering the Signatures of Shocks, Flux Ropes, and Prominences in Coronagraph Observations of CMEs. *Sol. Phys.*, *284*, 179-201. doi: 10.1007/s11207-012-0084-8

Vourlidas, A., Patsourakos, S., & Savani, N. P. (2019, July). Predicting the geoeffective properties of coronal mass ejections: current status, open issues and path forward. *Philosophical Transactions of the Royal Society of London Series A*, *377*(2148), 20180096. doi: 10.1098/rsta.2018.0096

Webb, D. F., & Howard, T. A. (2012, June). Coronal Mass Ejections: Observations. *Living Reviews in Solar Physics*, *9*(1), 3. doi: 10.12942/lrsp-2012-3

Weiss, A. J., Möstl, C., Amerstorfer, T., Bailey, R. L., Reiss, M. A., Hinterreiter, J., ... Bauer, M. (2021, January). Analysis of Coronal Mass Ejection Flux Rope Signatures Using 3DCORE and Approximate Bayesian Computation. *ApJS*, *252*(1), 9. doi: 10.3847/1538-4365/abc9bd

Weiss, A. J., Möstl, C., Davies, E. E., Amerstorfer, T., Bauer, M., Hinterreiter, J., ... Baumjohann, W. (2021, March). Multi point analysis of coronal mass ejection flux ropes using combined data from Solar Orbiter, BepiColombo and Wind. *arXiv e-prints*, arXiv:2103.16187.

West, J. L. (2004). The geostorm warning mission: enhanced opportunities based on new technology.

Wold, A. M., Mays, M. L., Taktakishvili, A., Jian, L. K., Odstrcil, D., & MacNeice, P. (2018, March). Verification of real-time WSA-ENLIL+Cone simulations of CME arrival-time at the CCMC from 2010 to 2016. *Journal of Space Weather and Space Climate*, *8*(27), A17. doi: 10.1051/swsc/2018005

Wood, B. E., & Howard, R. A. (2009, September). An Empirical Reconstruction of the 2008 April 26 Coronal Mass Ejection. *ApJ*, *702*(2), 901-910. doi: 10.1088/0004-637X/702/2/901

Zhang, J., Richardson, I. G., Webb, D. F., Gopalswamy, N., Huttunen, E., Kasper, J. C., ... Zhukov, A. N. (2007, October). Solar and interplanetary sources of major geomagnetic storms ( $Dst \leq -100$  nT) during 1996-2005. *Journal of Geophysical Research (Space Physics)*, *112*(A10), A10102. doi: 10.1029/2007JA012321